

Emergent Atomic Environments in Twisted Bilayer Graphene and Their Use in the Prediction of the Vibrational Properties

Dilara Ickecan^{1,*}, Yunus Emre Okyayli², Erdi Ata Bleda¹, Dogan Erbahar³

¹Marmara University, Dept. of Physics, 34722, Ziverbey, Istanbul, Turkey

²Gebze Technical University, Dept. of Physics, 41400, Gebze, Kocaeli, Turkey

³Dogus University, Faculty of Engineering, Dept. of Mechanical Engineering, Umraniye, 34775, Istanbul, Turkey

While Bernal stacked bilayer graphene bears two distinct atom types in its lattice, there exists no analytical framework addressing the number of atomic environments that emerge in twisted bilayer graphene superlattices. In this work, we have computationally analyzed 120 different twisted bilayer superlattices using descriptor functions to study the emergent local environments. Our study reveals that the number of atoms with unique local environments depend on the superlattice size linearly. Moreover, this linear dependence manifests itself on two distinct lines and this automatically suggests a new classification scheme based on the local environments. As a possible application, the use of local environments in the investigation of vibrational properties is discussed with respect to the existing literature. Molecular dynamics simulations are performed to calculate the phonon density of states of the 120 structures as well as the local phonon density of states of their individual atoms. The similarity of the contributions of local density of states coming from atoms with the same local environment is demonstrated. Local density of states of the atoms with unique local environments of an arbitrary selection of the structures is then used to train a machine learning model. This model is used to predict the phonon spectra of twisted bilayer structures. Performance of the trained model is discussed thoroughly via different selection of training and test sets, and it is shown that the model proves effective in predicting the vibrational properties of any given twisted bilayer structure. The possible applications of the generic method presented which reaches far beyond twisted bilayer graphene is also discussed.

Introduction. The moiré patterns observed in twisted bilayer graphene (TBLG) structures are optical fringe-like features that emerge as a result of rotation of layers with respect to each other around their common normal axis. A new periodicity is generally created which manifests itself in a supercell bearing the same 6-fold rotational symmetry of the underlying lattices. The mathematical properties of these rotational moiré lattices have gained interest following the observations of some novel physical phenomena in twisted structures. The studies on moiré lattices generally focus on topics such as nomenclature and classification schemes [1, 2], creation conditions [3] as well as relationships between some characteristic parameters like rotation angle [3], lattice mismatch [4, 5] and superlattice size. Also, most of the theoretical studies regarding the electronic and vibrational properties of twisted systems look to the effect of rotation on the reciprocal lattice to interpret the modifications of physical properties via the band structures [6-8].

Despite all the efforts, the relationships between even the most fundamental parameters lack analytical expressions. For example, the dependence of the lattice parameter on twisting angle demonstrates a chaotic character as presented in Fig. 1. The only identified analytical relationship between the two is the lower bound on the size of the supercell [3]. This relationship can be derived using commensurability conditions [9] and it is expressed as $N = 1/\sin^2\left(\frac{\theta}{2}\right)$ where N stands for the number of atoms in the supercell and θ for the twisting angle. One can also express this as a relationship between the lattice parameter (L) and the twisting angle θ as $L = 1.2295 \text{ \AA} / \sin\left(\frac{\theta}{2}\right)$ by using the areal atom density of bilayer graphene. This expression is represented by the red curve in Fig. 1. There are also studies which can incorporate the effect of lattice mismatch on lattice size in the case of two different layers [4, 5]. These studies all focus on the supercell itself characterizing the size, indexing, orientation, etc. and say nothing about the local features appearing in a given lattice.

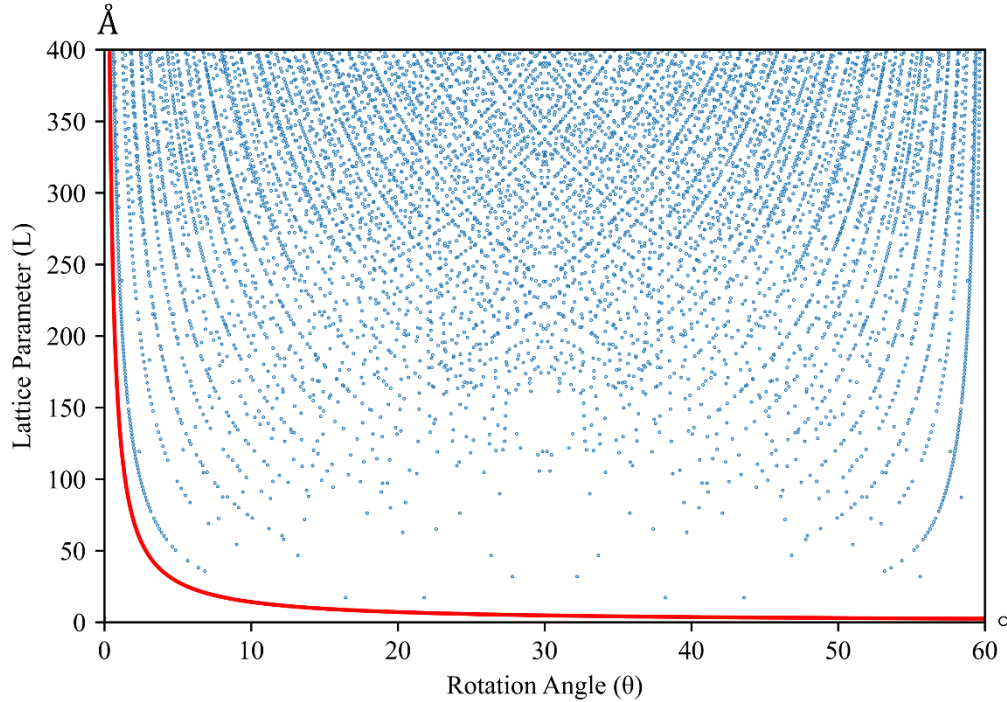


FIG. 1. (Color online) The dependence of lattice parameter on the twisting angle for 3447 moiré lattices appearing in TBLG. Each blue dot represents a moiré pattern with a unique rotation angle. The mirror symmetry of the plot around $\theta = 30^\circ$ line stems from the inherent 6-fold symmetry of the structures. Red curve is the lower bound on the lattice parameter.

However, we believe that in physical terms, the characterization of moiré superlattices by their local environments is crucial in making sense of their physical properties. In this regard, the emergent local environments of these superlattices can as well constitute a basis of a classification scheme. In this study, we survey this uncharted territory towards an understanding of the subpatterns and local environments as well as their effects on the physical properties.

Identification of local environments. First, it is important to note the empirical observation that the number of different atomic environments emerging in the superlattice is unique to the corresponding moiré pattern. To understand what is meant by this, let us first consider Bernal stacked bilayer graphene. This structure has two different “types” of atoms with respect to their local environments: one sitting exactly on top of an atom on the opposite layer and the second sitting in the midpoint of a hexagon of the opposite layer. The upper panel of Fig. 2(a) illustrates this by using different colors to distinguish the two types (Throughout this manuscript the expression “type” is used to refer to carbon atoms with a unique local atomic environment).

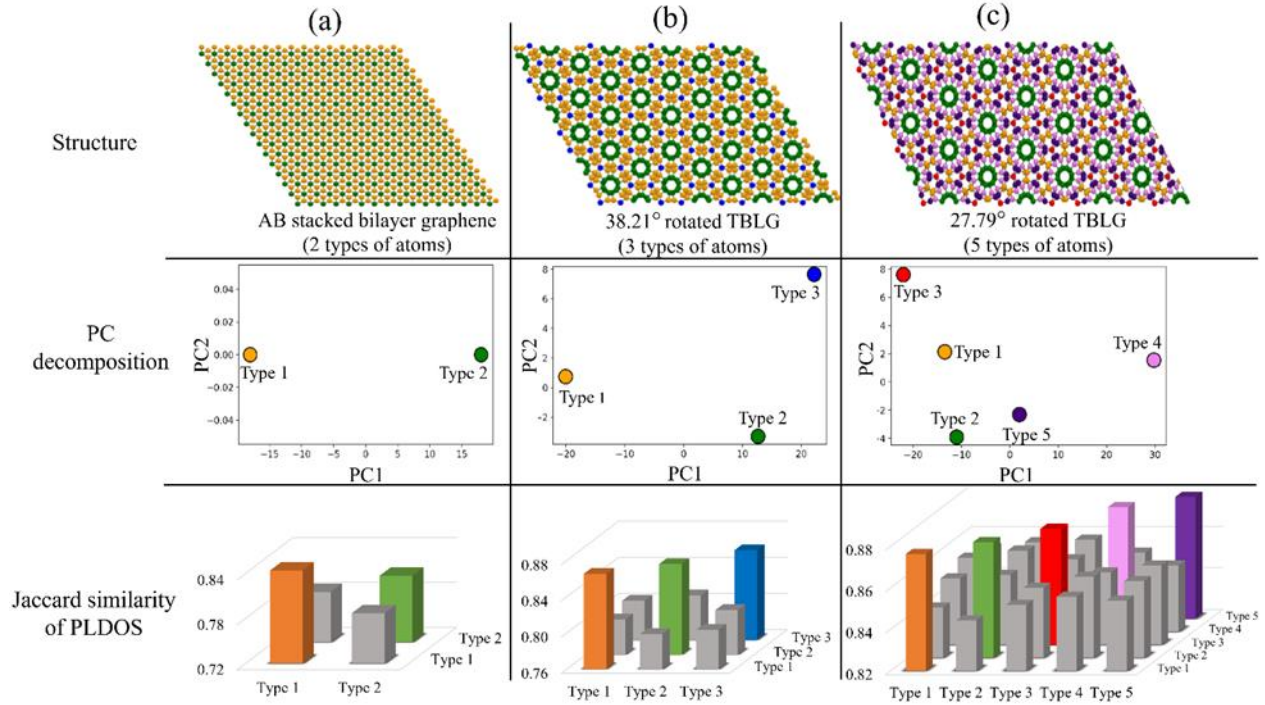


FIG. 2. (Color online) In the upper panel atoms are coloured according to their local environments in (a) Bernal stacked (b) 38.21° rotated and (c) 27.79° rotated TBLG's. Middle panel demonstrates the PCA of corresponding structures with SOAP descriptors. Lower panel shows the Jaccard similarity indices of phonon local density of states emerging from different types of atoms in the structure compared with each other.

Now, turning our attention to TBLG, one realizes that the situation immediately becomes non-trivial if not chaotic. A relatively manageable case is shown in the upper panel of Fig. 2(b) for the demonstration of the idea. Here, a moiré superlattice with a rotation angle of 38.21° is shown. One would identify 3 different types of atoms only after a careful visual inspection if it were not colored differently. 27.79° rotated TBLG in the upper panel of Fig. 2(c) stands out yet as a more complicated case where it becomes significantly harder to identify the 5 different types of atoms from the perspective of human pattern recognition. The determination of the number of different types of atoms in a general TBLG supercell is the first mathematical curiosity that we focus on, to which to our knowledge, there exists no explicit analytical solution.

Descriptor functions are extensively used in machine learning studies in condensed matter physics [10-12]. Due to their ability to capture rotation, translation, and permutation invariant atomic environments they might be particularly suitable for identifying and counting the emergent patterns in TBLG. Smooth Overlap of Atomic Positions (SOAP) descriptor [10] is one of the main descriptor schemes used in this regard and is chosen in this study to investigate the case thoroughly.

Middle panels of Fig. 2 (a), (b) and (c) demonstrate the ability of SOAP descriptors to verify the number of types in the corresponding structures via Principal Component Analyses (PCAs). These principal components are acquired from the descriptor matrices, and the corresponding scree plots indicate that the first 3 PCs are capable of capturing an overwhelmingly large portion of the data's variances. Convergence tests are performed and a resolution of three significant figures after decimal points is found to be a sufficient tolerance for separating different types in bigger structures. SOAP descriptor parameters used in this study are optimally selected as 10, 10 and 0.8 Å for n_{max} , l_{max} and σ , respectively. Here, n_{max} and l_{max} represent the highest degree of the radial and angular distribution functions while σ characterizes the smoothing between the atoms to match the typical range of interatomic interactions [13]. The cutoff radius of 30 Å is chosen since this value embraces at least half of the lattice parameter of the largest supercell used.

By applying this method to 120 different moiré lattices 21578 different types of atoms with different atomic environments are identified. The number of emergent types vs. the total number of atoms in each moiré supercell is presented in Fig. 3. The most significant feature of this plot is the grouping of 120 structures on two distinct lines. The R^2 values of the linear best fits are both greater than 0.99, which strongly supports the proposed linear model. While we don't have a full explanation for the existence of these two lines, the reciprocal values of their slopes seem to stem from the 6-fold rotational symmetry of them since the calculated reciprocal values of the slopes 5.94 and 35.0 are close to 6 and 6^2 .

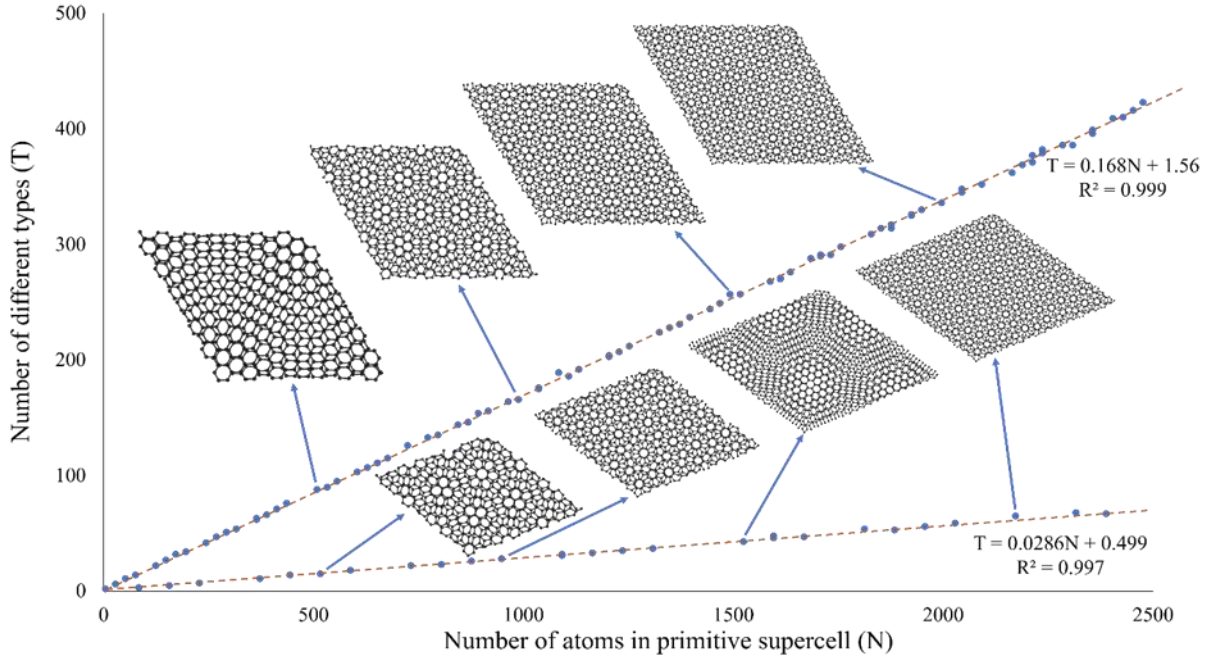


FIG. 3. (color online) The dependence of emerging types on the size of the supercell. The 120 investigated structures lie on two different nearly perfect lines. The slopes of the best fit lines are calculated as 0.168 and 0.0286 which correspond to 5.94 and 35 atoms in the cell per type respectively. Some randomly selected structures are also shown to point out the lack of any obvious pattern regarding the difference between two sets.

The possible existence of “higher order” lines which would have a reciprocal slope close to 216 (6^3) or 6^4 , etc. is a curiosity which might be chased by including more structures to the analysis. It is also worth to note that, none of the structures on the lines bear exactly the ratio of 6 or 36. This is due to the unique subpatterns emerging in each structure, where certain symmetrical groups and occasional overlaps contribute to the total number with different weights. The structures shown in the upper panel of Fig. 2(a), (b) and (c) have for example the respective ratios being 2, 28 and 31.2.

These two lines might be regarded as an indication of a new classification scheme of TBLGs with respect to their atomic environments. Some selected structures on both lines are also shown in Fig. 3 to point out that there are no obvious visual clues or recognizable patterns to indicate the class to which a given structure belongs.

The significance of the local environment analysis presented above becomes more pronounced when it finds applications in certain domains. In this regard, the problem we focus on is the prediction of the vibrational characteristics of any given TBLG. We approach this problem by decomposing the spectrum into contributions from atoms with unique local environments.

Phonons in TBLG. The intense focus on TBLG phonons has been triggered by the discovery of superconductivity in a “magic-angle” rotated sample in 2018 [14, 15]. While this discovery initiated the birth of *twistronics*, the nature of the superconductivity has been under debate since then with no decisive consensus [16-19]. Some studies attribute the superconductivity purely to unique electronic properties [20-23] while others refer to more conventional phonon

mediated behavior [24-27]. Hence, the vibrational characteristics of twisted bilayer structures have been one of the major research foci in the field [27-30].

Superconductivity however, is not the only reason for the interest in TBLG phonons since a complete understanding of the vibrational characteristics would have important implications for low-energy transport and collective phenomena [27]. Indeed, the analysis of the phonon spectra of TBLG has revealed soliton signatures, indicating the complex nature of phonon behavior in this material [31]. Moreover, layer-breathing phonons are recently shown to strongly couple to resonantly excited electrons in TBLG, with their resonance conditions being tunable by the twist angle [32].

First theoretical studies on TBLG phonons predicted that only minor changes would be expected to take place in low frequencies; however experimental results demonstrated a much richer picture throughout the spectrum. For example, G-band which is known to correlate with electron-phonon coupling was shown [33, 34] to change its half-width in near magic angles. While this was related to the emergence of flat bands, some experimental studies have also reported the appearance of new peaks in the Raman spectrum of TBLG for various twisting angles [35-38]. The theoretical and computational approaches to the topic are diverse. Here, we yet introduce a generic scheme of phonon total density of states (PTDOS) prediction from the phonon local density of states (PLDOS). This prediction is realized by a machine learning model which is trained by PLDOS data coming from the unique local atomic environments.

Calculating phonon spectra by molecular dynamics simulations. To produce this data, molecular dynamics (MD) simulations are performed on 120 TBLGs. Tersoff potential is used for modelling the interactions between carbon atoms in the same layer, while Lennard-Jones potential is employed for handling the van der Waals interactions between atoms in different layers. M. Wen, et al. [39] gives an extensive review of the potentials used in multilayer graphene simulations. It should be noted that none of the potentials in the literature are perfect for predicting the exact frequencies in phonon spectra. The potential scheme we have chosen gives the relative intensities and shape of the dispersion curve sufficiently good up to an arbitrary scaling factor in the frequency range. The simulations are run at room temperature and the fluctuation-dissipation theory is used to calculate the phonon dispersion via the observation of displacement of atoms [40]. LAMMPS [41] code is used to calculate the PLDOS for each atom in the structure, as well as the PTDOS.

Obviously, the same types of atoms are expected to contribute to PTDOS equally. However, due to the stochastic nature of our method, an inherent noise is always present in the phonon dispersion curves. To monitor the effect of this on the calculated spectra we have performed similarity analysis between the PLDOSs of different types of atoms. Lower panel of Fig. 2(c) shows the results of this analysis for corresponding structures above. Jaccard similarity index [42] is used for this comparison where 5 random atoms from each types are chosen and their PLDOSs are compared with each other. The averages of these similarities are shown in Fig. 2(c). Higher values in the diagonal elements of the matrices verify that different atomic environments would have unique contributions which can be meaningfully characterized above a certain noise level.

Training the model from local environment. Encouraged by this result, we train a Kernel Ridge Regression (KRR) model on taking on the task of predicting the PTDOS spectra of a given TBLG. Out of 120 TBLG structures, 96 of them are randomly selected as the training set, while the remaining 24 structures are reserved for testing the model. The entire procedure is repeated five times, each with a different randomization seed, to establish a higher level of confidence in the model's performance and consistency. Below, we present the results obtained from the best performing seed. The results from the other seeds as well as further relevant details about the KRR model have been presented in the supplemental materials of this manuscript [43].

16363 unique atomic environments are identified in the training set, and by furthest point sampling (FPS), 40% of these are selected to train the model using Scikit-learn [44] library. The structures in the test set produce 5215 different types of atoms. The distribution of the elements in both training and test sets projected on the principal components is shown in Fig. 4(a). The homogeneous coverage of the descriptor space shows that the region is evenly presented both in training and test sets. The trained model is used to predict the PLDOS of each atom in the test set and these are then used to construct PTDOS of the test structures. A typical example for 2.65° rotated TBLG is shown in Fig. 4(b) where a direct calculation from MD simulation is compared with the prediction of the model.

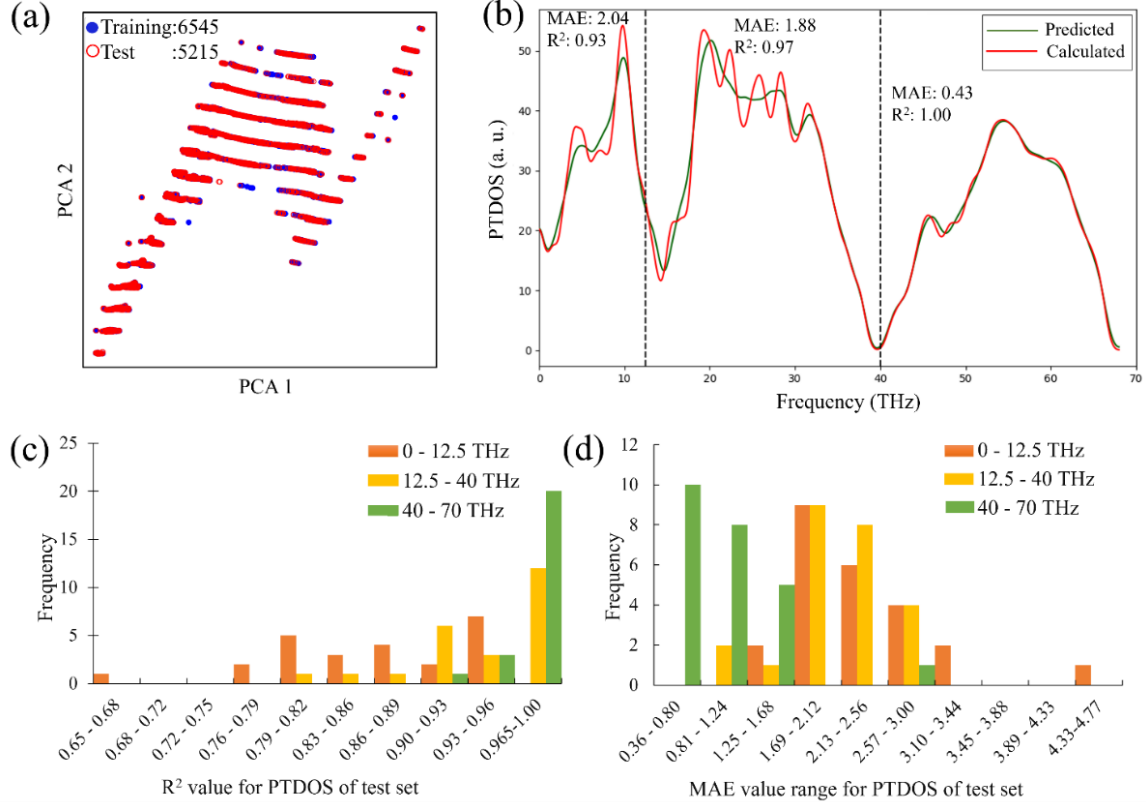


FIG. 4. (Color online) (a) Distribution of the elements in both training and test sets projected on principal components. (b) PTDOS of 2.65° rotated TBLG calculated from MD simulations vs. predicted from trained model. Accuracy of the prediction is calculated in three regions of the frequency domain. R^2 and mean absolute error (MAE) values are calculated and presented separately in each region. Histograms of (c) R^2 and (d) MAE values of 24 TBLG structures used in test set.

TBLG supercells investigated in the study have lattice parameters ranging from 7 \AA to 80 \AA . Taking the speed of sound in graphene as a reference, the frequency range of the phonons corresponding to that range has an order of magnitude of 0 to 1 in THz units. Phonons in this regime are expected to be more prone to be coupled to moiré periodicity and hence affected more by the twisting. Indeed, theoretical, and experimental studies in the literature focus generally on the low frequency end of the spectrum reporting modifications of the phonon spectra to some extent [26-28, 34]. To elaborate on this point, we have divided the PTDOS into three regions and separately studied the prediction accuracy of our model for each region. Fig. 4(b) shows that the R^2 and mean absolute error (MAE) values point to a higher accuracy towards the higher frequencies where these metrics slightly drop in the lower frequency regime. We attribute this to be the result of the richer variety in the lower frequency range of PLDOS where it becomes more challenging for the model to learn and predict. All R^2 and MAE values for the predicted PTDOS of 24 TBLG structures in the test set are shown in Fig. 4(c) and Fig. 4(d) as histograms. The same trend of Fig. 4(b) also appears here where the predictive power of the model drops towards lower frequencies. Still, the accuracy values reported in the long wavelength region are quite acceptable compared to the established standards in machine learning studies. The mean values of the MAE and R^2 values of the 24 structures in the test set are reported in TABLE I.

TABLE I. The mean values R^2 and MAE values of the structures used in test set.

Range (THz)	R^2	MAE
0 – 12.5	0.87	2.35
12.5 – 40	0.94	2.12
40 – 70	0.98	0.97

The results of the other four seeds are provided in the supplemental materials of this manuscript to demonstrate the relatively low fluctuation in these statistical indicators.

Concluding remarks. In this letter, we have addressed the question of identification of emergent atomic environments in TBLG which might serve as a basis to a novel classification scheme. The problem was beyond the reach of human pattern recognition and lacked an analytical solution. In this regard, it demonstrates an excellent example of how artificial pattern recognition could complement human insight. We have also presented an application of local environment decomposition to predict the vibrational spectra of TBLG structures. The generic method presented here for calculating the vibrational spectra can be generalized to any twisted bi- or multilayered structure as well as structures that bear strain induced moiré patterns. Furthermore, since focusing on the local environment removes the heavy restriction of periodicity which most of the computational methods suffer, this approach could easily be employed to study non-periodic structures like quasi crystals, amorphous materials, etc.

Acknowledgements. Authors would like to thank to Dr. Alberto Zobelli for useful discussions at the beginning of the project. We gracefully thank Prof. Savas Berber for discussions. DE would like to acknowledge the financial support from TUBITAK 1001 programme (project number: 122F022) and Dogus University scientific research project programme (project no: 2020-21-D2-B01). DI would like to thank TUBITAK 2211-C BIDEF programme for the scholarship. EAB would like to thank BAPKO of Marmara University for additional computation support. The simulations were partly performed on TUBITAK-ULAKBIM High Performance and Grid Computing Centre (TRUBA).

*Corresponding author: dilaraickecan@marun.edu.tr

- [1] A. Artaud, L. Magaud, T. Le Quang, V. Guisset, P. David, C. Chapelier, J. Coraux, Scientific Rep. 6, 25670 (2016)
- [2] M. Ciesler, D. West, S. Zhang, Journal of Applied Phys.134, 14 (2023).
- [3] J. M. Campanera, G. Savini, I. Suarez-Martinez, and M.I. Heggie, Phys. Rev. B 75, 235449 (2007).
- [4] S.S. Dindorkar, A.S. Kurade, A.H. Shaikh, Chem. Phys. Impact, 100325 (2023).
- [5] M. Yankowitz, J. Xue, D. Cormode, J.D. Sanchez-Yamagishi, K. Watanabe, T. Taniguchi, P. Jarillo-Herrero, P. Jacquod, B.J. LeRoy, Nature Phys. 8, 382 (2012).
- [6] J.-A. Yan, W. Y. Ruan, M. Y. Chou, Phys. Rev. B 77, 125401 (2008).
- [7] N. R. Chebrolu, B. L. Chittari, J. Jung, Phys. Rev. B 99, 235417 (2019).
- [8] R. Bistritzer, A.H. MacDonald, Proceedings of the National Academy of Sciences 108, 12233 (2011).
- [9] S. Shallcross, S. Sharma, E. Kandelaki, and O. A. Pankratov, Phys. Rev. B 81, 165105 (2010).
- [10] A. P. Bartók, R. Kondor, and G. Csányi, Phys. Rev. B 87, 184115 (2013).
- [11] M. Rupp, A. Tkatchenko, K.-R. Müller, and O. A. von Lilienfeld, Phys. Rev. Lett. 108, 058301 (2012).
- [12] J. Behler and M. Parrinello, Phys. Rev. Lett. 98, 146401 (2007).
- [13] T. Barnard, S. Tseng, J. P. Darby, A. P. Bartók, A. Broo, and G. C. Sosso, Mol. Syst. Des. Eng. 8, 300 (2023).
- [14] Y. Cao, V. Fatemi, A. Demir, S. Fang, S.L. Tomarken, J.Y. Luo, J.D. Sanchez-Yamagishi, K. Watanabe, T. Taniguchi, E. Kaxiras, Nature 556, 80 (2018).
- [15] Y. Cao, V. Fatemi, S. Fang, K. Watanabe, T. Taniguchi, E. Kaxiras, and P. Jarillo-Herrero, Nature 556, 43 (2018).
- [16] E. Codecido, Q. Wang, R. Koester, S. Che, H. Tian, R. Lv, S. Tran, K. Watanabe, T. Taniguchi, F. Zhang, Sci. Advances 5, eaaw9770 (2019).
- [17] Y. Cao, D. Rodan-Legrain, J. M. Park, N. F. Yuan, K. Watanabe, T. Taniguchi, R. M. Fernandes, L. Fu, and P. Jarillo-Herrero, Science 372, 264 (2021).
- [18] H. C. Po, L. Zou, A. Vishwanath, and T. Senthil, Phys. Rev. X 8, 031089 (2018).
- [19] M. Yankowitz, S. Chen, H. Polshyn, Y. Zhang, K. Watanabe, T. Taniguchi, D. Graf, A.F. Young, C.R. Dean, Science 363, 1059 (2019).
- [20] G. Tarnopolsky, A. J. Kruchkov, and A. Vishwanath, Phys. Rev. Lett. 122, 106405 (2019).

- [21] M. Koshino and N. N. T. Nam, Phys. Rev. B 101, 195425 (2020).
- [22] Y. W. Choi and H. J. Choi, Phys. Rev. Lett. 127, 167001 (2021).
- [23] Y. W. Choi and H. J. Choi, Phys. Rev. B 98, 241412(R) (2018).
- [24] F. Wu, A. H. MacDonald, and I. Martin, Phys. Rev. Lett. 121, 257001 (2018).
- [25] B. Lian, Z. Wang, and B. A. Bernevig, Phys. Rev. Lett. 122, 257002 (2019).
- [26] X. Liu, R. Peng, Z. Sun, and J. Liu, Nano Lett. 22, 7791 (2022).
- [27] M. Koshino and Y.-W. Son, Phys. Rev. B 100, 075416 (2019).
- [28] A. I. Cocemasov, D. L. Nika, and A. A. Balandin, Phys. Rev. B 88, 035428 (2013).
- [29] Z. Li, J.-M. Lai, and J. Zhang, Journal of Semiconductors 44, 011902 (2023).
- [30] D. L. Nika and A. A. Balandin, Reports on Progress in Phys. 80, 036502 (2017).
- [31] M. Lamparski, B. Van Troeye, V. Meunier, 2D Materials 7, 025050 (2020).
- [32] H. Hao, M.-L. Lin, B. Xu, H. Wu, Y. Wang, H. Peng, P.-H. Tan, L. Tong, J. Zhang, ACS Nano, (2023).
- [33] A. Schäpers, J. Sonntag, L. Valerius, B. Pestka, J. Straszdas, K. Watanabe, T. Taniguchi, L. Wirtz, M. Morgenstern, B. Beschoten, 2D Materials 9, 045009 (2022).
- [34] T. C. Barbosa, A. C. Gadelha, D. A. Ohlberg, K. Watanabe, T. Taniguchi, G. Medeiros-Ribeiro, A. Jorio, and L. C. Campos, 2D Materials 9, 025007 (2022).
- [35] A. Righi, P. Venezuela, H. Chacham, S. Costa, C. Fantini, R. Ruoff, L. Colombo, W. Bacsá, and M. Pimenta, Solid State Commun. 175, 13 (2013).
- [36] J. Campos-Delgado, L. G. Cancado, C. A. Achete, A. Jorio, and J.-P. Raskin, Nano Research 6, 269 (2013)
- [37] V. Carozo, C. M. Almeida, E. H. Ferreira, L. G. Cancado, C. A. Achete, and A. Jorio, Nano Lett. 11, 4527 (2011).
- [38] Y. Wang, Z. Su, W. Wu, S. Nie, N. Xie, H. Gong, Y. Guo, J. Hwan Lee, S. Xing, X. Lu, Applied Phys. Lett. 103 (2013).
- [39] M. Wen and E. B. Tadmor, Phys. Rev. B 100, 195419 (2019).
- [40] L. T. Kong, Comput. Phys. Commun. 182, 2201 (2011).
- [41] A.P. Thompson, H.M. Aktulga, R. Berger, D.S. Bolintineanu, W.M. Brown, P.S. Crozier, P.J. in't Veld, A. Kohlmeyer, S.G. Moore, T.D. Nguyen, Comput. Phys. Commun. 271, 108171 (2022)
- [42] T. T. Tanimoto, International Business Machines Corporation, (1958).
- [43] See supplemental material for details about the KRR model and result from each seeds, which includes Ref. [44, 45].
- [44] F. Pedregosa, G. Varoquaux, A. Gramfort, V. Michel, B. Thirion, O. Grisel, M. Blondel, P. Prettenhofer, R. Weiss, V. Dubour, The Journal of Machine Learning Res. 12, 2825 (2011).
- [45] K.P. Murphy, Machine learning: a probabilistic perspective, MIT Press (2012).

Supplemental Material: Emergent Atomic Environments in Twisted Bilayer Graphene and Their Use in the Prediction of the Vibrational Properties

Dilara Ickecan^{1,*}, Yunus Emre Okyayli², Erdi Ata Bleda¹, Dogan Erbahar³

¹Marmara University, Dept. of Physics, 34722, Ziverbey, Istanbul, Turkey

²Gebze Technical University, Dept. of Physics, 41400, Gebze, Kocaeli, Turkey

³Dogus University, Faculty of Engineering, Dept. of Mechanical Engineering, Umraniye, 34775, Istanbul, Turkey

[*dilaraickecan@marun.edu.tr](mailto:dilaraickecan@marun.edu.tr)

MACHINE LEARNING MODEL DETAILS

In this study, we employ the Kernel Ridge Regression (KRR) technique [1], a sophisticated machine learning method that combines ridge regression with kernel trick to enhance prediction accuracy in complex datasets. The KRR method is particularly advantageous in scenarios where the relationship between the variables is nonlinear. We opt for the Laplacian kernel, renowned for its efficacy in capturing locality and intricate structures in data. The Laplacian kernel, characterized by its exponential decay, is particularly suitable for datasets where identifying the local structure is crucial. Furthermore, the alpha parameter in the KRR was set to 0.01, a tuned choice aimed at achieving an optimal balance between model complexity and training data fit. This low alpha value suggests a strong regularization effect, mitigating the risk of overfitting while ensuring sufficient model flexibility to capture the underlying data patterns. The combination of the Laplacian kernel with this specific alpha setting in KRR underpins the robustness and accuracy of our predictive model, particularly in handling high-dimensional and complex data structures.

In this study, the R-squared (R^2) value is employed to survey the proportion of the variance in the dependent variable that is predictable from the independent variables. R^2 is defined as the square of the correlation coefficient between the observed and predicted values, mathematically expressed as:

$$R^2 = 1 - \frac{\sum(y_i - \hat{y}_i)^2}{\sum(y_i - \bar{y})^2}$$

where y_i represents observed values, \hat{y}_i denotes predicted values, and (\bar{y}) is the mean of observed values. This statistic is vital for evaluating the predictive strength of our model, indicating how well future data points are likely to be predicted. Concurrently, the mean absolute error (MAE) is utilized to measure the accuracy of predictions. MAE is calculated as the average of the absolute differences between the predicted and observed values, defined as:

$$MAE = \frac{1}{n} \sum |y_i - y'_i|$$

where n is the number of observations. MAE provides a straightforward metric to understand the average error magnitude in predictions, reflecting the typical deviation of predicted values from actual observations. Together, R-squared and MAE are instrumental in illustrating the efficiency and accuracy of our model in representing the physical phenomena under investigation.

RESULTS OF THE OTHER 4 RANDOMIZATION SEEDS

In the main text Fig. 4 shows the results of the best performing seed. Here in Fig. S1 we demonstrate the results for the other 4 seeds. A seed initiates the process of randomly choosing 96 structures for training set and leaving the remaining 24 for the test set. After the identification of unique atomic environments in the chosen structures, furthest point sampling (FPS) is used to select 40 % of these to train the model by Scikit-learn [2]. The structures in the training and test sets produce different number of types for each seed. These numbers are shown in Table S1.

TABLE S1. Number of identified atomic environments emerging from different randomization seeds. 40 % of the identified environments was chosen by furthest point sampling to train the model. The number of different environments in the structures that were reserved for test set is shown in the last column.

	Identified	Training	Test
SEED 1	16971	6788	4606
SEED 2	16986	6794	4590
SEED 3	17521	7008	4057
SEED 4	16851	6740	4726

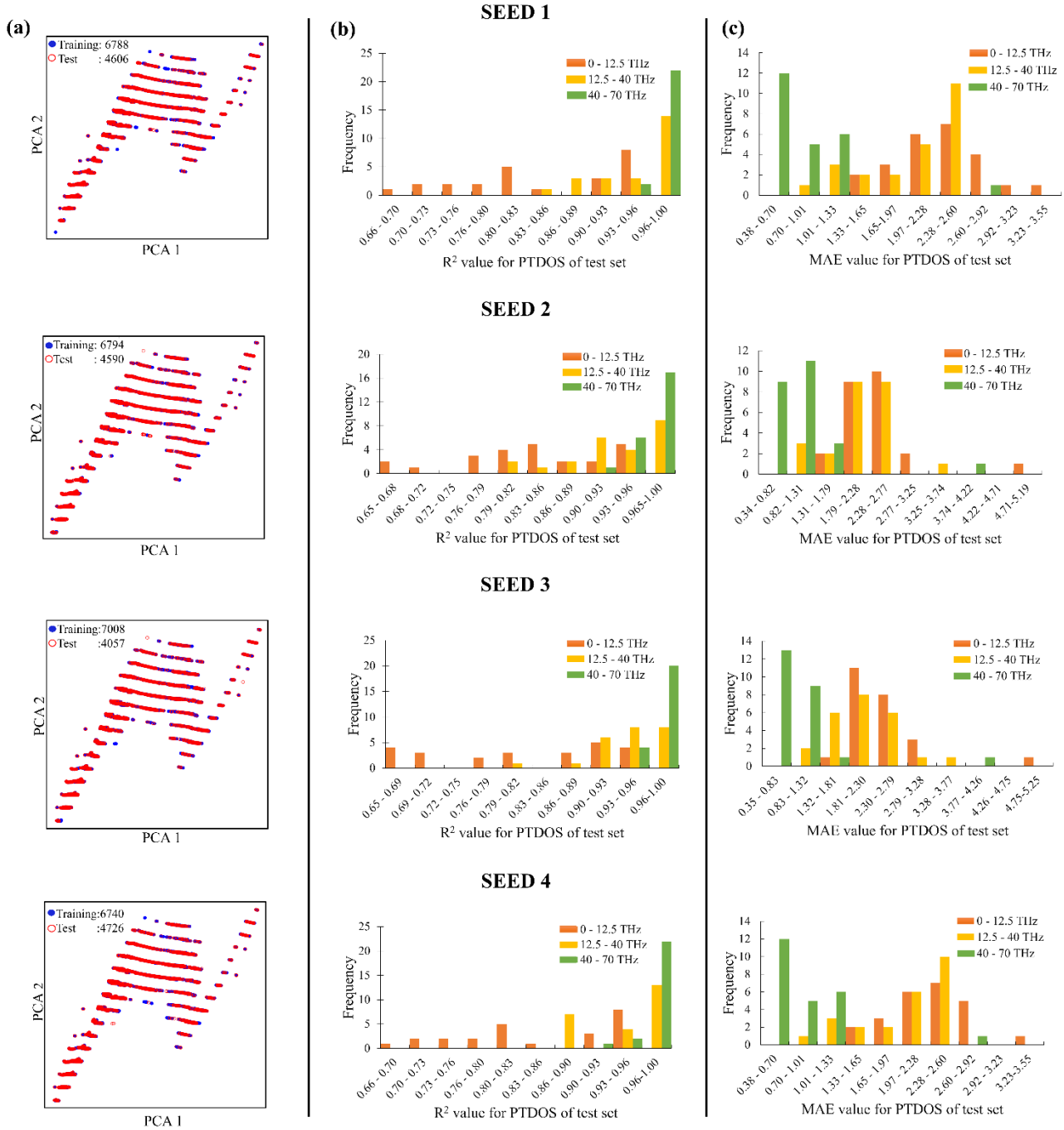


FIG. S1. (Color online) (a) Distribution of the elements in both training and test sets projected on principal components for different seeds. Histograms of R^2 (b) and MAE (c) values of predicted PTDOS of 24 TBLG structures in the test set for the respective seeds. The histograms are calculated for three regions of the spectra.

The distribution of the elements in both training and test sets projected on the principal components is shown in Fig. S1(a). The homogeneous coverage of the descriptor space by training set shows that in every seed the regions are evenly presented both in training and test sets which is a natural result of FPS algorithm that we employ. All R^2 and MAE values for the predicted PTDOS of 24 TBLG structures in the test set for other seeds are also shown in Fig. S1(b)-(c) as histograms.

The mean values of the R^2 and MAE of the 24 structures in the test set for the respective seeds are reported in Table S2.

TABLE S2. The mean values of R^2 and MAE of 24 TBLG structures used in test set for the respective seeds.

Range (THz)	SEED 1		SEED 2		SEED 3		SEED 4	
	R^2	MAE	R^2	MAE	R^2	MAE	R^2	MAE
0 – 12.5	0.85	2.21	0.84	2.41	0.82	2.44	0.85	2.31
12.5 – 40	0.94	2.04	0.93	2.17	0.94	2.05	0.95	1.98
40 – 70	0.98	0.76	0.97	1.04	0.98	0.92	0.98	0.85

The mean values of the MAE and R^2 values for all 5 seeds as well as their respective variances are given in Table S3.

TABLE S3. The mean values and variances of R^2 and MAE of all 5 seeds.

Range (THz)	R^2	Variance in R^2	MAE	Variance in MAE
0 – 12.5	0.85	0.000240	2.35	0.007
12.5 – 40	0.94	0.0000278	2.07	0.004
40 – 70	0.98	0.0000098	0.91	0.009

[1] K.P. Murphy, Machine learning: a probabilistic perspective, MIT Press (2012).

[2] F. Pedregosa, G. Varoquaux, A. Gramfort, V. Michel, B. Thirion, O. Grisel, M. Blondel, P. Prettenhofer, R. Weiss, V. Dubourg, The Journal of Machine Learning Res. 12, 2825 (2011).